Science Advances
AAAS

Manuscript Template

FRONT MATTER

Title

- Landscapes buried beneath large-volume ignimbrites reveal pre-eruptive uplift rates
- Uplift rates revealed beneath large ignimbrites

Authors

Byron A. Adams,[1,2]* Frances J. Cooper,[1,2] Clementine Walsh,[2] Katharine V. Cashman,[2,3]

Affiliations

[1]Department of Earth Sciences, University College London, London, UK.

[2]School of Earth Sciences, University of Bristol, Bristol, UK.

[3]Department of Earth Sciences, University of Oregon, Eugene, Oregon, USA.

*Corresponding author. Email: byron.adams@ucl.ac.uk

Abstract

Pyroclastic density currents associated with large explosive volcanic eruptions can generate expansive ignimbrite deposits characterized by planar, low-angle surfaces. We demonstrate the utility of these surfaces for constraining pre-eruptive rock uplift rates based on the relief of the paleo-landscapes buried beneath them. Using a landscape evolution model driven by river erosion, we explore the range of permissible landscape geometries beneath an ignimbrite of a given surface slope. Our results demonstrate a clear correlation between river channel steepness and the overall slope of the topography, as a function of rock uplift rate. We show that lower rock uplift rates are generally required to generate gentle landscapes that can be buried by ignimbrite deposits. Model application to the Early Miocene Cardones ignimbrite on the western flank of the Central Andes yields pre-eruptive rock uplift rates of <0.26 km Myr^{-1}, comparable with independent thermochronometric and geothermobarometric constraints.

Teaser

Surface slopes of large-volume ignimbrite deposits record pre-eruptive rock uplift rates of landscapes buried beneath them.

MAIN TEXT

Introduction

Subduction zones along convergent plate boundaries host some of Earth's largest mountain ranges and most explosive volcanoes. Because these high-elevation regions persist over long timescales, they provide important settings for evaluating orogen-building processes (*1*, *2*), orogenic influences on regional and global climate (*3–5*), and interactions between volcanism and landscape evolution (*6*). Understanding the evolution of a mountain range requires knowledge of its rock uplift history. However, rock uplift rates are difficult to determine over long time scales.

Long-term uplift rates can be assessed using the history of surface uplift, which occurs when the rock uplift rate exceeds the exhumation rate (the rate at which material is removed from the surface by erosion or faulting). Surface uplift rates can be estimated from changes in elevation derived from stable isotope compositions of precipitates or biota (*3*). Alternatively, rock uplift rates can be equated with exhumation rates if surface uplift is assumed to be negligible. Most constraints on exhumation rely on geochemical proxies such as thermochronometric cooling histories (*7*) or tied geobarometric and geochronologic constraints (*8*, *9*).

Most long-term constraints on rock uplift rates rely on indirect proxies such as thermochronometric cooling histories or geobarometric estimates, which require numerical models to translate primary observations into surface-referenced velocities. These approaches have yielded critical insights into orogenic development, but their temporal resolution is limited by the spatial distribution and closure temperatures of the available data.

More broadly, relatively few conceptually distinct constraints on long-term rock uplift rates exist outside thermochronology and a small number of surface uplift estimates. This lack of independent tests makes it difficult to evaluate uplift histories over the timescales required for landscapes to adjust to tectonic forcing. Here, we explore a geomorphic approach that uses the geometry of landscapes buried beneath large-volume ignimbrites to provide a complementary constraint on pre-eruptive rock uplift rates, integrated over landscape response timescales.

We describe a method for constraining rock uplift rates in tectonically active volcanic regions where landscapes have been buried beneath large-volume, spatially-expansive ignimbrites. Rather than yielding an instantaneous uplift rate at a single point in the past, this approach constrains the range of rock uplift rates that could have acted over the time required for a landscape to develop prior to burial. The key observable is the planar, low-angle surface characteristic of ignimbrite deposits, which places a geometric limit on the relief of the buried paleo-landscape and thus on the uplift rate integrated over the landscape response time. Starting with the assumption that topographic relief is set by the geometry of river channel networks, we run a landscape evolution model with a form of the stream-power river incision model (*10*) to demonstrate how rock uplift rate fundamentally controls the slope of the mountain range orthogonal to the range crest (Fig. 1). Using this framework, we quantify how combinations of rock uplift rate and erodibility control range-scale slope, apply these relationships to landscapes buried by the Cardones ignimbrite, and compare the resulting uplift-rate bounds with existing geological and geomorphic constraints.

The paper proceeds in four steps. We first describe the geometry and emplacement of large-volume ignimbrites and establish the geometric constraints they impose on buried landscapes. We then introduce a simplified stream-power framework to link river network geometry, fluvial relief, and range-scale slope. Using two-dimensional landscape evolution models, we quantify how combinations of rock uplift rate and erodibility control the range-scale slopes compatible with ignimbrite burial and apply these results to the Miocene Cardones ignimbrite of the Central Andes. Finally, we discuss the implications of these constraints for rock uplift rate histories and orogenic evolution.

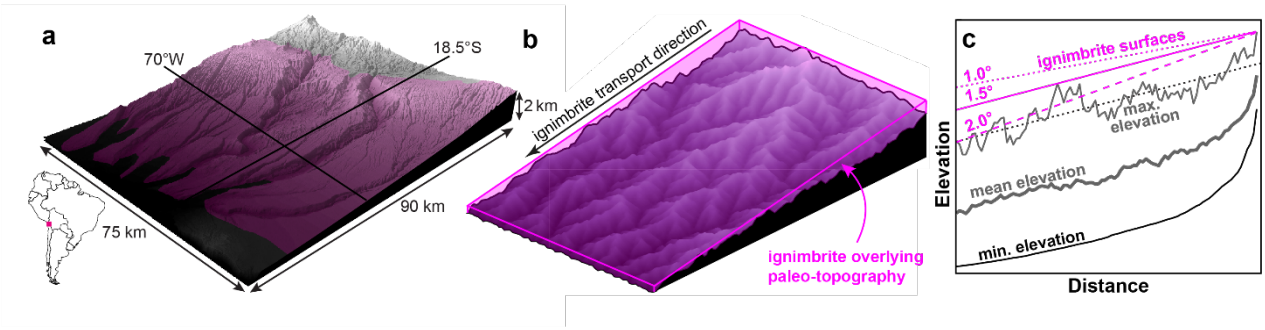

Fig. 1. Burial of a mountainous landscape beneath a large-volume ignimbrite. (a) Oblique view of the western Andes of southern Peru and northern Chile. The portion of the landscape colored in

magenta denotes the extent of Oligocene-early Miocene ignimbrite deposits (simplified from Garcia et al. (*11*)). (b) A synthetic landscape overlain by an ignimbrite deposit defined by a plane dipping 1.5° in the direction of transport. (c) Minimum, mean, and maximum elevation profiles of the synthetic landscape beneath the ignimbrite parallel to the transport direction. Black dotted line shows the regression of the maximum elevation profile, which we refer to as the range-scale slope. Magenta lines depict ignimbrite surface slopes of 1.0°, 1.5° (shown in b), and 2.0°.

Explosive volcanic deposition

Ignimbrite deposits

Ignimbrites are matrix-supported, pumice-dominated volcanic deposits created by pyroclastic density currents (PDCs) (*12*). Smaller ignimbrites (~10^{-1}–10^{1} km^3) are generally created by dome collapse (*13*), whereas large-volume deposits (10^2–10^3 km^3) result from PDCs triggered by the collapse of Plinian eruption columns or formation of large calderas (*14*). Many of the largest ignimbrite deposits were deposited during large eruptions (M > 8 using the scale of Mason et al. (*15*)) which may have originated from complex calderas typical of volcano-tectonic depressions, and are often transported > 100 km from their source (*16*, *17*). While small-volume eruptions typically produce valley-confined ignimbrites, the largest caldera-forming eruptions can create regionally extensive deposits defining large areas of uniform topography with a gentle slope. These are referred to as low aspect ratio ignimbrites (LARIs) (*18*) (Fig. 1). The thickness of a LARI deposit can often exceed 1 km, but will vary with the topography of the paleo-landscape buried beneath it, i.e. it will be thicker over a paleo-valley than over a paleo-ridge (*6*, *19*).

The modern morphology of a LARI surface is an expression of the initial deposit surface combined with any post-eruption deformation, erosion, or deposition of materials as surface processes such as river erosion and hillslope transport were re-established. The initial morphology of the surface is controlled by the discharge rate of the eruption, the pre-existing surface topography, and the fluidized state of the flow (*20*). Many LARI deposits form relatively flat, expansive surfaces with a gentle slope (0.5°–3°) that dips away from the source vent, causing the deposit to thin down-dip (*6*). Local deviations from this pattern can occur due to interaction with pre-existing topography, flow impoundment, or ponding, leading to spatially variable deposit thickness. However, such effects primarily influence local thickness distributions and do not generally reverse the large-scale slope of the ignimbrite surface. Because our analysis is based on the regional envelope of maximum ignimbrite elevations, rather than local thickness variations, these second-order effects do not undermine the geometric constraints imposed by ignimbrite burial.

Examples from around the globe with well-constrained initial slopes of 0.5°–3° include: The Valley of Ten Thousand Smokes ignimbrite (Alaska, USA) (*18*), Minoan ignimbrite (Santorini, Greece) (*21*), Kurile Lake ignimbrite (Kamchatka, Russia) (*22*), Ito deposit (Aira, Japan) (*23*), Toba Tuff (Indonesia) (*24*), Zaragoza ignimbrite (Los Potreros, Mexico) (*25*), Bishop Tuff (Long Valley, USA) (*26*), Huckleberry Ridge tuff (western USA) (*27*), and Cerro Galan ignimbrite (Argentina) (*28*).

If we assume that the source of the volcanic deposit must be higher than the landscape it engulfs, then three simple relationships are possible between the ignimbrite surface and the underlying topography (Fig 1b). (1) The ignimbrite surface is steeper than the range-scale slope of the buried landscape, consistent with the observation that ignimbrite deposits generally thin away from the source but are likely to produce a partially buried landscape where higher ridges and peaks protrude. (2) The ignimbrite surface is less steep than the buried surface, which is not likely over large distances since it requires ignimbrites to thicken away from their source. (3) The ignimbrite surface slope is approximately equal to the range-scale slope of the underlying landscape, such that burial of the paleo-topography represents a limiting case in which the deposit only just overtops the highest elevations. The key conclusion from these three scenarios is that to completely bury a

landscape beneath an ignimbrite, the slope of the maximum elevations of the paleo-topography must be equal to or less than the slope of the initial ignimbrite surface (Fig. 1c).

The steepest landscape that can be completely buried by a given ignimbrite is determined by a simple geometric criterion based on relative slopes, rather than on assumptions about ignimbrite volume or thickness. We represent both the ignimbrite surface and the pre-eruption landscape by their regional, range-scale envelope slopes projected over the same profile length. Complete burial is possible only if the slope of the ignimbrite surface is equal to or less than the slope of the maximum-elevation envelope of the paleo-topography. If the paleo-topographic envelope is steeper, the two surfaces intersect upstream and complete burial cannot occur. Thus, the case where the two slopes are nearly equal represents a near-threshold condition in which the ignimbrite only just succeeds in burying the landscape (Fig. 1c).

The Cardones Ignimbrite, Central Andes

The western margin of the Central Andes, straddling the border between northern Chile and southern Peru, is defined by a magmatic arc that has evolved in response to continuous subduction of the Farallon plate beneath South America since the early Jurassic (*29*). Over time, explosive volcanism has blanketed much of the region, most notably during a volcanic flare-up in the early Miocene caused by steepening of the subducting slab after a period of flat slab subduction (*30*). This is marked by deposition of the Oxaya Formation, a regionally extensive series of gently west-dipping ignimbrites, the largest of which – the 21.9 Ma Cardones ignimbrite (>1,260 km^3) – is thought to have been sourced from the nearby Lauca Caldera (*17*, *19*). van Zalinge and others (*6*) determined that the Cardones ignimbrite originally had a relatively uniform surface slope of 1.5 ± 0.3°, making it a prime example of a LARI deposit. This estimate incorporates the post-deposition folding and tilting that is recorded in their reconstructed drill core transect. Before applying this approach to the Central Andes, we first establish the theoretical relationship between fluvial relief, channel steepness, and range-scale slope using a simplified stream-power framework.

Controls on contractional orogen relief

LARI deposits make useful datums because of their large spatial extent and the precise age control offered by radiometric techniques such as U-Pb and $^{40}Ar/^{39}Ar$ geochronology (*31*). We use the slope of the Cardones LARI surface to constrain the (now-buried) pre-eruption topography. We then use the relief of that topography to infer the uplift rate that created it. Given our assumption that a buried landscape must be less steep than the deposit overlying it, there should be a definable limit to the rock uplift rate that formed the landscape prior to eruption. To test this idea, we used a landscape evolution model for the evolution of river networks to create synthetic landscapes, which we then compare with the current Cardones ignimbrite topography. The purpose of this section is not to exhaustively explore stream-power formulations, but to establish the minimum theoretical framework required to interpret ignimbrite burial as a constraint on range-scale relief.

To assess the influence of rock uplift rate on the relationship between fluvial relief and mountain range slope, we start with the conservation of mass and the classical stream-power model of river erosion (*32*, *33*):

$$\frac{dz}{dt} = U(x,t) - K(x,t)\, A(x,t)^m\, S(x,t)^n \qquad (1)$$

where $\frac{dz}{dt}$ is the surface uplift rate (z is the elevation of a river bed in meters, t is time in years, x is river distance in meters), U is the rock uplift rate (m yr^{-1}), and K (units depend on m; when $m = 1$, the units are m^{-1} yr^{-1}) is the coefficient of erosion, often referred to as erosional efficiency or erodibility. K encapsulates the integrated influence of environmental conditions such as climate, lithology, and factors that modulate erosional efficiency (e.g., roughness, sediment availability, and hydraulic conditions), A is the drainage area (m^2), S is the channel slope, and m and n are

dimensionless exponents related to runoff variability, channel erosion processes, and hydraulic geometry.

In steady-state landscapes – used here to mean erosion and rock uplift are approximately balanced and topography is invariant over time (i.e., $\frac{dz}{dt} = 0$) – stream power model predictions agree with the observation that local channel slopes are inversely proportional to drainage area (*34*, *35*) and, in natural landscapes, erosion rates scale as a power function of channel slope and drainage area (*33*). As a result, steady-state river channels produced by the stream-power model, and those found in nature, have concave-up forms that make it difficult to discern spatially limited changes in local channel slope that are critical to understanding river processes. To counteract this effect, local channel slopes can be adjusted for the downstream increase in drainage area using the relationship

$$S(x) = k_{sn}(x)\, A(x)^{\theta}, \quad (2)$$

where θ is a dimensionless constant that denotes the concavity of a longitudinal river profile and the coefficient, k_{sn}, is the channel steepness (*34*, *36*). Channel steepness can be measured by regression of a χ-plot, a linearized channel profile in which longitudinal distance is replaced by the integral of upstream accumulation area (χ) (*37*):

$$k_{sn} = \frac{z(x)}{\chi(x)} \quad (3)$$

$$\chi(x) = \int_0^x \left(\frac{A_0}{A(x)}\right)^{\theta} dx, \quad (4)$$

where A_0 is a reference area (1 m^2 in this study) used to simplify the units of the integral. To compare channel steepness values from different landscapes it is necessary to use a single θ value, referred to as θ_{ref}. When θ_{ref} is implemented in a suite of landscapes, the term *normalized channel steepness* (k_{sn}) is used. Here all channel steepness values are calculated with θ_{ref}, and are referred to simply as *channel steepness*. Quasi-steady-state landscapes with spatially uniform lithology, climate, and rock uplift rates, have a single channel steepness value, with a concavity equal to the ratio of m and n from the stream-power model (i.e., $\theta = m/n$) (*32*). To link the steepness of river channels to rock uplift rates, we combine equations 1 and 2 to find:

$$k_{sn} = \left(\frac{U}{K}\right)^{\frac{1}{n}}. \quad (5)$$

Equation 5 shows that channel steepness is directly proportional to rock uplift rate and inversely proportional to erodibility, such that mountain ranges with high rock uplift rates and low erodibility will be steeper and have greater relief than ranges with low rock uplift rates and high erodibility.

Here we consider only the development of fluvial relief, which typically comprises at least 80% of the range-scale relief (*38*, *39*) in non-glaciated orogens. Adding hillslope processes would significantly increase model complexity without greatly increasing accuracy. Additionally, using only the stream-power model allows us to constrain the development of range-scale relief with the fewest number of unconstrained variables. Because this simplified landscape evolution model does not include hillslope relief, plausible outputs of fluvial relief and channel steepness are likely to be maxima.

Erodibility of bedrock river channels

Measuring the erodibility of rocks in a river channel requires an accurate history of recent erosion. The most common method for estimating erodibility uses the stream-power model (eq. 1) to calculate local erosion rates by comparing the form of a modern channel with a paleo-channel of known age. From these rates and the measured values of S and A, m, n, and K can be estimated by minimizing the misfit between observed and modelled channel profiles (*40–42*). Erodibility can vary by several orders of magnitude between different rivers, even when m and n are held constant (*40*). When the effects of rock type are isolated, however, the erodibility of relatively competent (harder) versus relatively incompetent (softer) rocks may vary by only one order of magnitude (*43*,

44). Higher precipitation rates also increase erodibility (*43*, *45*, *46*) in tectonically active orogens, including in the Himalaya, where erodibility may scale proportionally with mean annual precipitation. In this way, high precipitation rates can subdue topographic relief, potentially masking high rock uplift rates (*45*).

Non-linearity of the stream-power model

Equation 5 shows the power-law dependency of rock uplift rates and erosion rate (when $U = E$) on channel steepness. In steady-state landscapes, the ratio m/n is equal to the concavity of river channel profiles, so some combination of n, m, and K values should fit the relationship of E or U, and channel steepness. Although concavity values in natural systems generally vary between 0.35 and 0.65, with most values close to 0.5 (*47*), inversion of river channel profile data yields highly variable n values even though a consistent regional value might be expected (*40*, *48*). Investigations of the problem from a regional perspective have used relationships between channel steepness and basin-average erosion rates derived from cosmogenic nuclides (i.e., equation 5) to constrain n (*48–51*). Regressions of erosion rates and channel steepness suggest that n varies between ~1 and 2 (*48*, *51–53*).

2-Dimensional model framework

We use the slope of maximum elevations (the range-scale slope, S_R) to summarize the geometry of our modeled landscapes because this slope is the limiting factor that determines whether a landscape can be completely buried by an ignimbrite. Range-scale slope is calculated from maximum elevations as a function of distance from the front of the model from a simplified swath profile (Figs. 1 and 2) using a least-square linear regression. Since river networks have a complex plan-form geometry (channel topology) and an along-river distance greater than the range-perpendicular distance, range-scale slope must be determined numerically. Channel topology, in turn, is critical for developing realistic drainage divides from which range-scale slope can be calculated.

Our 2D model uses the framework provided by Landlab (*54*), an open-source, Python-based toolkit for simulating surface processes. We do not seek to constrain a full suite of model parameters to explain any specific topography. Instead, we synthesize landscapes that can be used to quantify relationships between range-scale slope, channel steepness (k_{sn}), erodibility (K), and rock uplift rate (U).

Initial experiments were performed on a 22.4 × 22.4 km (~500 km^2) regular grid of 200 m node spacing with one open boundary (Fig 1b). To reduce the time required to reach steady-state topography and to make the relief metrics more comparable between different simulations, we initialized each model with the same elevation dataset, which included a river channel network with a total relief of 10 m. We do this to fix the steady-state topology for resulting landscapes. For each experiment we assumed a spatially and temporally uniform rock uplift rate and erodibility (see GitHub link for full codes in Jupyter Notebooks). We allowed the landscape to evolve until a steady-state topography was reached, indicated by stable channel steepness, stable erosion rates in space and time, and erosion rates equal to the imposed rock uplift rate.

We varied rock uplift rates between 0.1 and 2 km Myr^{-1} and erodibility from 1 x 10^{-9} to 1 x 10^{-6} m^{-1} yr^{-1} to produce 560 synthetic landscapes. The choice of single values of erosional efficiency and rock uplift rate are not indicative of assumed known geologic simplicity, but it is a clear way of using a sensitivity analysis to explore parameter space. Later in this section we explore the outcomes of relaxing these initial assumptions of uniformity. We also tested different initial channel topologies but found this did not affect the resulting topographic metrics. We used $n = 2$ and $m = 1$ for all model runs as values of $n > 1$ are most appropriate in tectonically active settings, and we expect the value of m/n to be around 0.5 (*45*, *51*, *52*, *55*). First-order results, however, do not rely on the values of m or n, if m/n is constant and comparable to natural landscapes. In detail, the non-

linear dependence of erosion rate on slope (i.e., $n = 2$) will affect the fluvial relief for a given K value. In other words, $n = 2$ requires smaller values of K than $n = 1$ to produce natural topographies at the same rock uplift rate (Fig. S1). This demonstrates the stream-power model requirement to have balanced n, m, and K values when comparing synthetic and natural landscapes.

Constraining non-steady-state topographies

Above we described a framework for using a 2D landscape evolution model to synthesize steady-state topographies formed by combinations of rock uplift rate and efficiency values, and below we will show that we can sample a reasonable range of these values using hundreds of model simulations. Conversely, it is much more difficult to synthesize the infinite possibilities of non-steady-state topographies that could span the same range of elevations as the steady-state landscapes. This endeavor requires a different approach to efficiently test millions of variable combinations.

To accomplish this, we first constrain the steepest topography that could be completely buried by a given ignimbrite using our 2D model output, which we represent on a linearized channel profile (χ-plot) (see Fig. 2 green datasets). This linearized profile is our comparator plot. We then create millions of more complex river profiles with convexities and concavities (knickpoints) whose elevations cannot be greater than that of the comparator plot. The spatial changes in channel steepness that create these non-uniform profiles could be the result of spatial or temporal changes in rock uplift rates of climate conditions such as rainfall. We create these profiles by making quasi-random linearized profiles with specific geometric forms, such as a profile containing one convex knickpoint, but not prescribing the length or steepness of the segments that make up the profile. We perform this 1D randomization technique millions of times for different geometric channel forms to create millions of linearized profiles and calculate the mean channel steepness for each simulated river (see Materials and Methods for details). Each simulation is forced to cover the full elevation range of the comparator plot to allow for the highest possible mean channel steepness values. We use the output of these simulations to affirm that the mean channel steepness and mean rock uplift rate recorded in a river profile will still be related (i.e., eq. 5) in transient conditions. In landscapes where m and n are uniform over space and time, variations in river profile concavity reflect spatial variations in channel steepness, which reflect changes in rock uplift rate over space and time.

Results

Relative influence of erodibility and rock uplift rate on range-scale slope

From the resulting steady-state topography of each K and U combination, we calculate the channel steepness and range-scale slope. Critically, varying n within the commonly inferred range (e.g., $n = 1–2$) alters the inferred erodibility required to match a given landscape geometry but does not change the uplift-rate bounds imposed by the ignimbrite surface slope (Fig. S1). Note that the resulting values of channel steepness are unitless because we use the χ method and a concavity value of 0.5 to calculate channel steepness. For a given K, U is proportional to channel steepness and range-scale slope (Fig. 2). Because $n > 1$, linear changes in rock uplift rate induce non-linear changes in topographic relief.

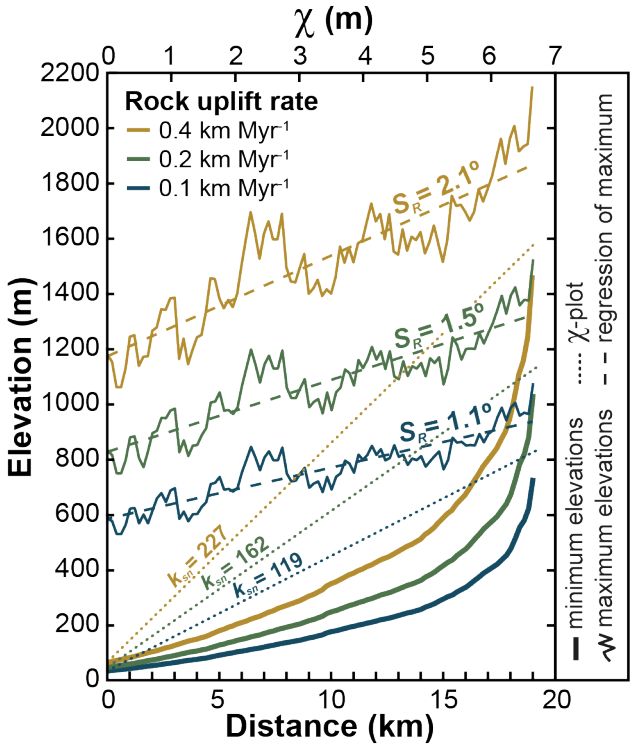

Fig. 2. Swath profiles from three 2D synthetic landscapes with the same erodibility (K = 8 x 10^{-9} m^{-1} yr^{-1}) and different rock uplift rates. These swaths collapse the topographies of the entire model domain. The minimum elevation, maximum elevation, regression of the maximum elevation (range-scale slope, S_R), and χ-plot (channel steepness, k_{sn}) are shown for each landscape. Note that the minimum elevation curves do not equate to longitudinal river profiles as river distance and range-scale distance are not the same.

Range-scale slope is linearly related to channel steepness (Fig. 3a) because the relationship is sensitive only to the ratio of our fixed m and n values. Figure 3b shows the contours of channel steepness and range-scale slope as a function of varying erosional efficiency and rock uplift rate. The relationship allows us to calculate an analytical solution for a range-scale slope given a U and K pair defined by equation 5 (thin, dashed lines in Fig. 3b). Low rock uplift rates and erodibility values cause contours to converge toward U = 0 km Myr^{-1}. Higher rock uplift rates cause the contours to become roughly parallel while higher erodibility values increase the distance between the contours.

Channel steepness (k_{sn}) provides a convenient, scale-normalized measure of fluvial relief, but its meaning is not always intuitive outside a river profile context. For reference, the $k_{sn} \approx 162$ trunk-channel example in Fig. 2 corresponds to ~1000 m of fluvial relief over ~18 km of range-perpendicular distance. Importantly, this relief does not directly equal the total mountain range relief (≈1400 m), because range-scale slope is not controlled by the trunk channel alone. Tributary networks contribute additional relief at multiple positions along the range, and drainage-divide geometry/topology therefore influences the maximum-elevation envelope used to define range-scale slope. This mismatch explains why range-scale slope cannot be inferred from a one-dimensional fluvial profile and motivates our use of two-dimensional landscape evolution models to relate channel-scale metrics to range-scale geometry.

To bury a landscape beneath an ignimbrite, the initial depositional surface slope of the ignimbrite must be equal to or greater than the range-scale slope of the landscape. Therefore, for the Cardones ignimbrite, where S_R = 1.5° (*2*), we explore a suite of landscapes with range-scale slopes ≤ 1.5°. This low-slope topography restricts plausible solutions for combinations of rock

uplift and erodibility to those above the 1.5° contour in Fig. 3b; to narrow the range of possible rock uplift rates plausible erosional efficiency must also be constrained.

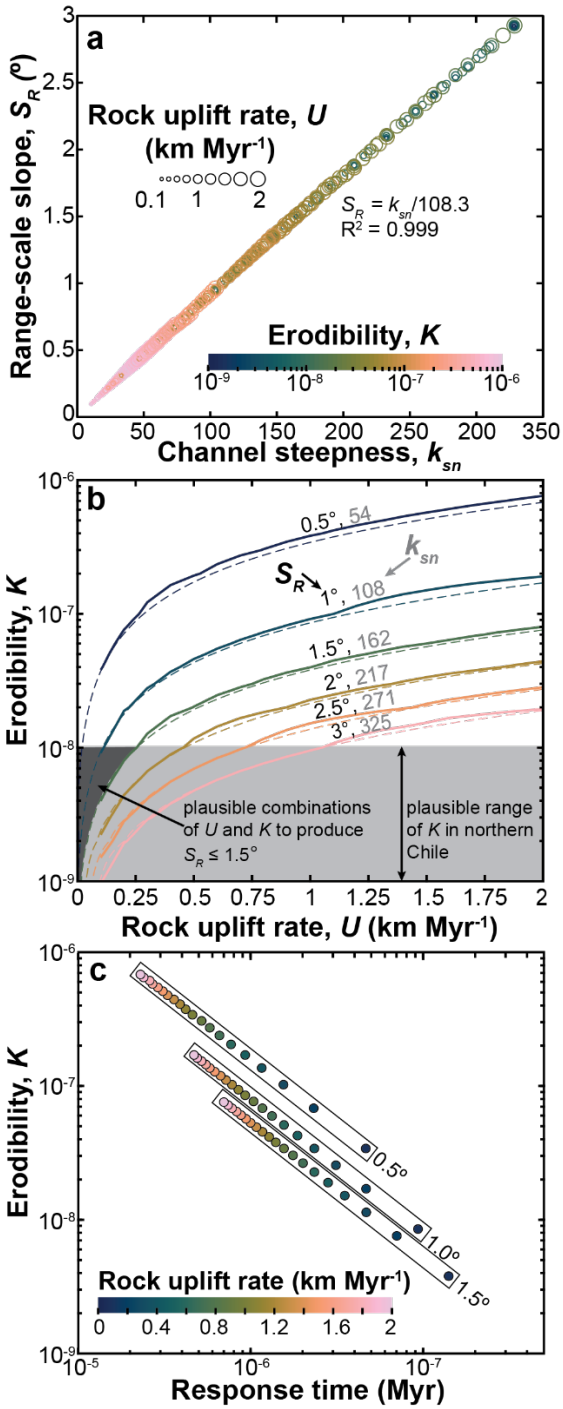

Fig. 3. Results of 2D landscape evolution modelling. (a) Comparison of channel steepness and range-scale slope (S_R) from each model simulation (560 in total) as a function of rock erodibility. For clarity, only simulations where $S_R < 3.0°$ are shown. See Fig. S2 for full results. The slope of the relationship, $S_R = k_{sn}/108.3$, is set by the river concavity. (b) The variability of range-scale slope from each combination of erodibility and rock uplift rate. Thick lines are contours of constant range-scale slope (S_R; values in black) and channel steepness (k_{sn}; values in gray) through the landscape evolution model output and thin, dashed lines are analytical solutions from equation 5. Contours of model output, instead of all model solution points, are shown for clarity. The dark gray wedge denotes the plausible rock uplift rates for range-scale slopes less than 1.5° and erodibility values

less than 1 x 10^{-8} m^{-1} yr^{-1} (light gray box). (c) Landscape response times increase strongly with decreasing erodibility and uplift rate, indicating that low-relief landscapes buried by ignimbrites require long-lived, low uplift rates.

Constraints from existing estimates of erodibility

Rock uplift rates within our synthetic landscape can be further constrained using estimates of erodibility from previous studies of natural landscapes. To normalize these erosional efficiency values to a consistent choice of stream-power exponents ($n = 2$ and $m = 1$), and ensure comparability with our model results, we apply the normalization approach of Barnhart et al. (*56*) (Table S1) and use the resulting values throughout the remainder of this paper. Stock and Montgomery (*40*) estimated erodibility of 2 x 10^{-9} to 2 x 10^{-8} m^{-1} yr^{-1} for rivers traversing granites and metasedimentary rocks in south-eastern Australia, and 3 x 10^{-9} to 5 x 10^{-9} m^{-1} yr^{-1} for rivers traversing basalts in Kauai (USA). Re-analysis of the Australian field area byvan der Beek and Bishop (*42*) yielded erodibility values of ~2 x 10^{-9} m^{-1} yr^{-1}. Studies of Himalayan igneous- and sediment-derived metamorphic rocks report a similarly broad range(~2 x 10^{-9} to 1 x 10^{-8} m^{-1} yr^{-1}), although this range may reflect spatially variable precipitation rather than rock properties (*45*).

Applying the scaling relationships of Adams et al. (*45*) together with geologic evidence for arid conditions in the Central Andes by Miocene time (*57*), suggests a representative regional erodibility of ~1 x 10^{-9} m^{-1} yr^{-1}. In addition, the very presence of the Miocene ignimbrites provides plausible values of erodibility, given that (i) the river network has struggled to remove the ignimbrite deposits over the last ~22 Myr and (ii) there are knickpoints at least 11 Myr old in the western Andes (*58*, *59*). These observations show that timescales of response are long and erodibility values must be low (i.e., Fig. 3c). Indeed, Fox et al. (*60*) invert modern topography to suggest an erodibility value of 8 x 10^{-9} m^{-1} yr^{-1} for the western flank of the Peruvian Andes. Because post-Miocene erosion rates in the region are exceptionally low, any erodibility values inferred from modern denudation data would imply lower rock uplift rates than those explored here; our adopted erodibility range therefore represents a conservative upper bound for pre-eruption conditions.

By stating that rivers have struggled to remove ignimbrite material, we refer to the long-term persistence of ignimbrite deposits on interfluves and canyon walls, and to the incomplete re-excavation of pre-eruption topography over tens of millions of years, rather than to short-term vertical incision through the deposits. This behavior distinguishes large-volume ignimbrites from many other volcanic disturbances, such as tephra falls, lava flows, or debris avalanches, which may locally perturb hydrology or incision but typically act over more limited spatial extents and shorter timescales. Our focus here is therefore on ignimbrites as regionally extensive, long-wavelength geomorphic perturbations that impose durable constraints on range-scale landscape geometry, rather than on the detailed dynamics of post-eruption landscape adjustment.

If we use these constraints to take a conservative one order of magnitude estimate of plausible erodibility values (1 x 10^{-9} to 1 x 10^{-8} m^{-1} yr^{-1}), rock uplift rates are constrained to <0.26 km Myr^{-1} for topographies with slopes $\leq 1.5°$ (Fig. 3b). This suggests that the pre-eruption landscapes buried by ignimbrites on the western Andean margin were of relatively low relief (k_{sn} ~160) due to the relatively low rock uplift rate, as compared to other modern active orogens. An order of magnitude range of erodibility values is sufficient for this study to adequately constrain rock uplift rate given the form of the modeled uplift–slope relationships, but need not be adequate in all settings.

Constraining timescales of landscape response

The time required for a river network to adjust to a change in rock uplift rate depends on the characteristic length scale over which adjustment must occur. Because landscape response is ultimately governed by the distance over which knickpoints must migrate, we performed an additional suite of model runs at larger spatial scales (100 × 50 km) to obtain response times more

representative of long Andean river systems during the Early Miocene. For these simulations we used analytical solutions for erodibility values (Fig. 3b), rock uplift rates of 0.1 to and 2 km Myr^{-1}, and range-scale slope values of 0.5°, 1.0°, and 1.5°. These models were also initiated with a landscape containing an established river network and a maximum relief of 10 m. As the adjustment between two steady-states follows an exponential temporal path in our models, we report the timescale of response where the landscape has achieved 95% of the expected relief rather than 100%, which can take considerably longer despite the insignificant difference in topography (*61*). Figure 3c demonstrates the effect of rock uplift rate, erodibility, and final topographic relief on the timescale of response. The landscapes with the lowest erodibility, lowest rock uplift rate, and highest final relief take the longest to achieve a new steady state following a change in rock uplift rate.

Assessing complex topographies in 1D

Our sensitivity analysis of longitudinal river profiles using χ-plot randomization shows that any complex channel with a profile that can plot beneath a uniform, steady-state river profile must have a mean channel steepness value less than the steady-state river (Fig. 4). We also show that more complex profiles have a lower channel steepness than a steady-state profile, when the overall relief of the profile is conserved. This demonstrates that the uniform, steady-state condition represents the maximum channel steepness and can be used as a conservative end member to constrain maximum rock uplift rates.

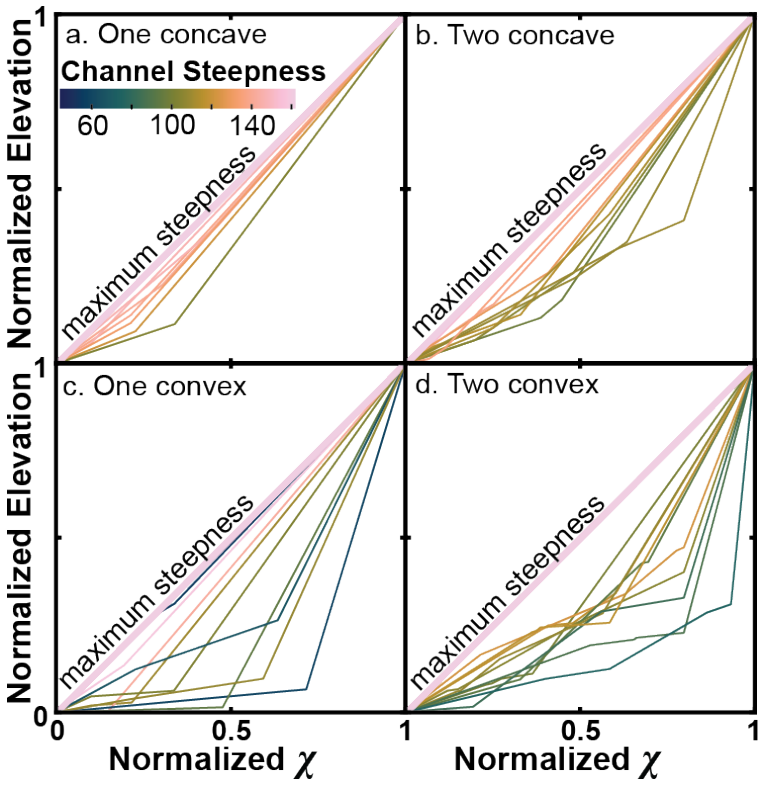

Fig. 4. Complex river profiles from 1D χ-plot randomization. Ten simulations from a population of three million are shown in each panel, colored by mean channel steepness value (see Fig. S3 for histograms of all simulations). The thicker pink bounding line represents the maximum steepness value (k_{sn} = 162) shown in Fig. 3b. (a) Profiles with one concave knickpoint. (b) Profiles with two concave knickpoints. (c) Profiles with one convex knickpoint. (d) Profiles with two convex knickpoints. Increasing geometric complexity increases the overall profile concavity and decreases the mean channel steepness.

Discussion

Can the stream-power model describe buried landscapes?

While the stream-power model might appear overly simplistic for addressing complex problems of river erosion and the geometry of unobservable landscapes, it can describe the broad geometry of mountainous landscapes. Moreover, our focus on the range-scale slope means that our results do not depend on either the model space dimensions or the river channel topology. Furthermore, our use of channel steepness as a measurement of fluvial relief means that the precise values of m and n do not matter if their ratio lies within the expected landscape limits (i.e., knowing the concavity is more important than knowing m or n). Previous work has shown that 0.46 is an appropriate concavity for rivers on the western Andean margin in northern Chile (*59*), and sits in the middle of observed values from other natural landscapes (*47*). We therefore suggest that values of $n = 2$ and $m = 1$, to yield a concavity of 0.5, provide a reasonable and conservative estimate for landscape modelling.

The relationship between range-scale slope and fluvial relief within our dataset is controlled primarily by river channel concavity, although the expected relationship between any measurement of relief and rock uplift rate or erodibility will change as a function of n (eq. 5). For example, $n = 1$ predicts a linear relationship between channel steepness and rock uplift rate, whereas $n = 2$ predicts a non-linear relationship such that increasing rock uplift rate increases channel steepness as $U^{0.5}$ for a constant K. Because K, n, and m are inter-related, however, Fig. 3 holds an accurate guide to considering rock uplift rates in any landscape where $m/n \approx 0.5$.

Could the buried landscapes have non-uniform topographies?

Since the pyroclastic density currents responsible for transporting ignimbrites are fluidized flows that travel downslope, thickness variations in the resulting deposits often record large-scale topographic perturbations. For example, we might expect a PDC emplaced onto a landscape defined by steep vent-proximal reaches and gentler downslope portions to show a similar change in the surface of the ignimbrite in addition to downslope thickening, as seen in the ignimbrite resulting from the ~7.7 ka eruption of Mt Mazama (Crater Lake), Oregon, USA (*62*). Similarly, we anticipate the upper surface of an ignimbrite to record a change from a proximate shallow slope to a more distal steeper portion of the landscape. That said, the important characteristic of an ignimbrite datum is an expansive surface that can be approximately described by a single surface slope, and that the deposit thins in a predictable manner away from the source. If these conditions hold, then minor perturbations in the paleo-topography that are not discernible in the ignimbrite surface are unlikely to reduce the accuracy of our estimates of rock uplift rate.

When compared to steady-state landscapes with uniform boundary conditions, non-steady or non-uniform landscapes will have different geometries (Fig. 4) that can be defined by a change in concavity, where the concavity of the landscape is no longer directly related to the ratio of m and n but instead represents a change in channel steepness over space and time at constant m and n. Enhanced concavity in both river channel (Fig. 4b) and gross topographic profile can develop in landscapes that experience a decrease in rock uplift rate over time or where erodibility values are higher at lower elevations. Spatially variable rock uplift rates can also change the apparent concavity of a landscape, whereby landscapes become more concave when rock uplift rates increase toward the range crest and vice versa (*59*, *63*). Conversely, temporal increases in either rock uplift rate or erodibility can induce large-scale convexities (convex up; Fig. 4c) in both river channels and gross topographic profiles (*64*, *65*). The extent to which such topographic variations can be buried by an ignimbrite such as the Cardones, with its final slope of 1.5°, limits the overall steepness and long-term rock uplift rate.

Implications for rock uplift rates in the Central Andes

Interpreting these uplift-rate constraints in the context of prior erosion and exhumation estimates requires recognizing the strong temporal variability of erosion on the western margin of the Central Andes. Several studies have suggested higher denudation rates during the Miocene followed by a pronounced decline associated with the onset of extreme aridity (*66*), while modern catchment-averaged cosmogenic nuclide data indicate exceptionally low present-day erosion rates across the region (*67*). Both paleo-denudation reconstructions and modern erosion rates integrate over fundamentally different timescales and depend sensitively on model assumptions and climate histories. Importantly, the ignimbrite-based constraints presented here do not rely on adopting specific paleo- or modern erosion rates; instead, they bound the average rock uplift rate acting over the landscape response time required to generate the buried topography prior to ignimbrite emplacement.

Our analysis suggests that the western margin of the Central Andes in northern Chile experienced relatively low rock uplift rates before the Miocene volcanic flare-up. The low-relief topographies buried beneath the Oxaya Formation ignimbrites are similar to lower elevation portions of modern contractional orogens including the eastern Andean fold-and-thrust belt (*68*), the physiographic Lower Himalaya of central Nepal (*69*), and large portions of Taiwan (*70*). Despite having much higher rock uplift rates and erosion rates on the order of 4-6 km Myr^{-1} (*71*), Taiwan is thought to have much higher erodibility values, resulting in lower relief landscapes. By contrast, the Lower Himalaya and portions of the Andean fold-and-thrust belt have relatively low rock uplift rates due to shallowly dipping faults.

Our model-derived uplift rates cannot be directly compared with those derived from thermochronology and geobarometry studies because of different integration timescales. Most low-temperature thermochronometric cooling ages on the western Andean margin are Eocene, yielding time-averaged rock uplift rates from ~50 Ma to the present of < 0.2 km Myr^{-1} (*72*). Our rock uplift rate estimate of <0.26 km Myr^{-1} is integrated over the much shorter time period required for the landscape to reach steady state. The length of our model domain and the initial river relief of 10 m produce a mountain range with a range-scale slope of 1.5° within ~14 Myr (at 95% steady-state), with $K = 4 \times 10^{-9}$ m^{-1} yr^{-1} and $U = 0.1$ km Myr^{-1}. Here, the time to steady-state is inversely proportional to K. However, we note that ~14 Myr is an approximate estimate for how much time may have been required for steady rock uplift rates to create a steady-state landscape, and steady rates could have persisted for longer. Low-temperature thermochronometry constraints on uplift rates from the Late Cretaceous/Paleocene to present have suggested low rock uplift rates similar to the <0.26 km Myr^{-1} reported here (*72*) whereas, exhumation rates that integrate over the Incaic orogeny (~55-40 Ma) are >0.25 km Myr^{-1} (*9*). The consistency of our shorter-term constraint over only ~14 Myr with longer-term constraints from thermochronology suggest a relatively steady tectonic history since the Incaic, and confirm that the Miocene-Pliocene Quenchua orogeny was mostly limited to Peru and did not significantly impact northern Chile (*73*, *74*).

The requirement that ignimbrites bury landscapes formed under relatively slow pre-eruptive rock uplift rates can be viewed in the broader context of orogenic evolution. Periods of tectonic stabilization or waning deformation allow sufficient time for river networks to reorganize and for range-scale relief to decrease, whereas phases of rapid or spatially variable uplift are unlikely to generate low-relief landscapes over comparable distances. Similar relationships between low-relief landscapes and slowed or reorganized tectonic forcing have been documented in other orogenic settings (*65*). In this framework, ignimbrite burial does not imply a causal relationship between uplift and volcanism, but rather reflects a geomorphic selectivity: regionally extensive ignimbrites preferentially preserve landscapes that developed during specific tectono-magmatic states of an orogen. Ignimbrites therefore act as long-wavelength geomorphic markers that sample particular phases of orogenic evolution, rather than arbitrary snapshots of uplift history. **Conclusions**

Like other expansive and datable depositional or erosional surfaces, low aspect ratio ignimbrites provide valuable datums for constraining paleo-topographies and the boundary

conditions that formed them. Because ignimbrites generally taper away from their source and form an upper surface described by a gentle slope, there is a limited suite of landscape geometries that can lie beneath them. These geometric constraints, coupled with a broad understanding of landscape erodibility, can be used to constrain tectonic histories. Importantly, ignimbrites that preserve a relatively low surface slope must cover relatively low relief landscapes. Low relief landscapes, in turn, can result from low rock uplift rates and commensurate low erosion rates, high erodibility values due to the prevalence of easily eroded bedrock, or high precipitation rates.

Using the initial surface geometry of the large-volume Miocene Cardones ignimbrite on the western margin of the Central Andes and the theory of the stream-power model, we have constrained average Oligocene-Miocene rock uplift rates to a maximum of 0.26 km Myr^{-1}. These results provide a robust independent constraint on the development of the Central Andes aligned with existing thermochronometric and geothermobarometric constraints and consistent with a period of relatively slow subduction zone convergence.

We have used the Central Andean Miocene flare-up as a case study in this paper, but the lessons learned are broadly applicable to other regions that preserve large-volume ignimbrites. Our modelling results provide a framework to constrain the paleo-topographies buried beneath other low aspect ratio ignimbrites, provided there is good reason to suggest the river networks would have had concavity values close to 0.5. The transferability of our method could be improved with more precise values of m and/or n. Landscape modelling experiments would also improve our understanding of volcanic landscapes, particularly the relationship between eruption discharge, topographic roughness, and ignimbrite thickness or runout and improve estimates of ignimbrite volumes by predicting paleo-topographies and the rates and patterns of post-eruption erosion. Taken together, our results indicate that regionally extensive ignimbrite burial preferentially records landscapes shaped during periods of relatively slow or spatially uniform uplift. This suggests that ignimbrite surfaces are not generic markers of orogenic uplift, but instead sample tectono-magmatic states in which landscapes have sufficient time to equilibrate prior to burial. More broadly, ignimbrite burial provides a geomorphic filter on uplift histories, highlighting specific phases of orogenic evolution rather than the full range of tectonic conditions.

Materials and Methods

Calculation of time to steady-state

The calculation of time to steady-state (t) is difficult in synthetic and real landscapes as minor fluctuations in forcing factors or minor numerical instabilities may preclude a landscape from being 100% stable. In addition, the non-linear propagation of erosion signals over time often results in perhaps unreasonable estimates of time to steady-state, whereby considerable amounts of time are spent waiting for the last few meters of the highest relief areas to finish adjusting. Therefore, it is common to assume some threshold by which the landscape is functionally in steady-state without every square meter being stable. For our purposes, we assume steady-state when the mean erosion rate of the new landscape has reached 95% of the modelled rock uplift rate. Where t satisfies the equation:

$$0.95 = \bar{E}(t)/U \quad (6)$$

Calculation of χ-plot randomization

To constrain the range of longitudinal river profiles compatible with a prescribed maximum fluvial relief, we generate synthetic χ-profiles using a randomized, rule-based construction in χ-elevation space. The χ coordinate is defined following the stream-power formulation and is calculated using Hack's Law (*35*)

$$L = cA^h \quad (7)$$

where the exponent, h, was set to 0.6 and the coefficient c was set to 4.53×10^{-1} to achieve a channel steepness value of 162 for the initial steady-state χ-plot. We used values of $m = 1$, $n = 2$, $\theta = 0.5$ for consistency with our 2D models. We created randomized χ-plot using four rules.

1) The left end point of the lowest segment was set to $z_1 = 0$ and $\chi_1 = 0$. The right end point was found by randomly selecting a χ value and then using a channel steepness value between 1 and 162 to calculate a new elevation value at the selected χ (i.e., eq. 3).
2) If the boundary between the previous segment and the next segment was to be a concave knickpoint, the next segment needed to have a greater channel steepness. The left endpoint of this segment was set to be the right endpoint of the previous segment. The right endpoint was determined by picking a new χ value and selecting a new elevation bounded by a minimum value calculated using the channel steepness of the previous segment and a maximum value set by the elevation of the initial steady-state profile at the selected χ value.
3) If the boundary between the previous segment and the next segment was to be a convex knickpoint, the next segment needed to have a lower channel steepness. The left endpoint of this segment was set to be the right endpoint of the previous segment. The right endpoint was determined by picking a new χ value and selecting a new elevation bounded by a minimum channel steepness value of 1 and a maximum channel steepness set by the previous segment.
4) The last segment was calculated by finding the required channel steepness value to connect the right endpoint of the previous segment with the maximum χ and elevation values from the initial steady-state χ-plot.

These rules were repeated millions of times with varying combinations of knickpoints to produce the data shown in Fig. 4 and S3. See GitHub site for full code.

Geometric interpretation of χ-plot randomization.

Although χ is parameterized using Hack's law and stream-power exponents to define the steady-state χ–z reference profile, the χ-plot randomization is used here to sample admissible longitudinal geometries subject to a fixed maximum fluvial relief. All synthetic profiles are constrained to share the same maximum χ and elevation values defined by the steady-state profile; variation among realizations reflects only the redistribution of slope along the profile through different combinations of concave and convex knickpoints. Varying Hack's law coefficients or exponents rescales χ and the associated channel-steepness values, but does not alter the relief-limited envelope that governs the range-scale slopes used to constrain uplift rates. As a result, uplift-rate bounds derived from the χ-randomization are controlled by the imposed geometric limits rather than by the specific choice of length–area scaling parameters. This approach allows efficient sampling of admissible longitudinal geometries consistent with a fixed maximum fluvial relief, without requiring assumptions about transient discharge variations or time-dependent incision processes.

References

1. S. D. Willett, Orogeny and orography: The effects of erosion on the structure of mountain belts. *Journal of Geophysical Research-Solid Earth* **104**, 28957–28981 (1999).

2. P. G. DeCelles, M. N. Ducea, P. Kapp, G. Zandt, Cyclicity in Cordilleran orogenic systems. *Nature Geosci* **2**, 251–257 (2009).

3. C. N. Garzione, G. D. Hoke, J. C. Libarkin, S. Withers, B. MacFadden, J. Eiler, P. Ghosh, A. Mulch, Rise of the Andes. *Science* **320**, 1304–1307 (2008).

4. C. J. Poulsen, T. A. Ehlers, N. Insel, Onset of Convective Rainfall During Gradual Late Miocene Rise of the Central Andes. *Science* **328**, 490–493 (2010).

5. S. Lamb, P. Davis, Cenozoic climate change as a possible cause for the rise of the Andes. *Nature* **425**, 792–797 (2003).

6. M. E. van Zalinge, R. S. J. Sparks, L. A. Evenstar, F. J. Cooper, J. Aslin, D. J. Condon, Using ignimbrites to quantify structural relief growth and understand deformation processes: Implications for the development of the Western Andean Slope, northernmost Chile. *Lithosphere* **9**, 29–45 (2017).

7. P. W. Reiners, M. T. Brandon, Using Thermochronology to Understand Orogenic Erosion. *Annual Review of Earth and Planetary Sciences* **34**, 419–466 (2006).

8. E. J. F. Mutch, J. D. Blundy, B. C. Tattitch, F. J. Cooper, R. A. Brooker, An experimental study of amphibole stability in low-pressure granitic magmas and a revised Al-in-hornblende geobarometer. *Contrib Mineral Petrol* **171**, 85 (2016).

9. S. I. R. Dahlström, F. J. Cooper, J. Blundy, S. Tapster, J. Cortés Yáñez, L. A. Evenstar, Pluton Exhumation in the Precordillera of Northern Chile (17.8°–24.2°S): Implications for the Formation, Enrichment, and Preservation of Porphyry Copper Deposits. *Economic Geology*, doi: 10.5382/econgeo.4912 (2022).

10. J. Braun, S. D. Willett, A very efficient O(n), implicit and parallel method to solve the stream power equation governing fluvial incision and landscape evolution. *Geomorphology* **180–181**, 170–179 (2013).

11. M. García, M. Gardeweg, J. Clavero, G. Hérail, Arica map: Tarapacá Region, scale 1: 250,000. *Carta Geológica de Chile Serie Geología básica* **84** (2004).

12. G. P. L. Walker, Grain-Size Characteristics of Pyroclastic Deposits. *The Journal of Geology* **79**, 696–714 (1971).

13. R. A. F. Cas, J. V. Wright, "Ignimbrites and ignimbrite-forming eruptions" in *Volcanic Successions Modern and Ancient* (Springer Netherlands, Dordrecht, 1988; http://link.springer.com/10.1007/978-94-009-3167-1_8), pp. 222–266.

14. R. S. J. Sparks, L. Wilson, A model for the formation of ignimbrite by gravitational column collapse. *Journal of the Geological Society* **132**, 441–451 (1976).

15. B. G. Mason, D. M. Pyle, C. Oppenheimer, The size and frequency of the largest explosive eruptions on Earth. *Bull Volcanol* **66**, 735–748 (2004).

16. S. D. Silva, G. Zandt, R. Trumbull, J. G. Viramonte, G. Salas, N. Jiménez, Large ignimbrite eruptions and volcano-tectonic depressions in the Central Andes: a thermomechanical perspective. *Geological Society, London, Special Publications* **269**, 47–63 (2006).

17. E. S. Platzman, R. S. J. Sparks, F. J. Cooper, Fabrics, facies, and flow through a large-volume ignimbrite: Pampa De Oxaya, Chile. *Bull Volcanol* **82**, 8 (2019).

18. G. P. L. Walker, Ignimbrite types and ignimbrite problems. *Journal of Volcanology and Geothermal Research* **17**, 65–88 (1983).

19. M. E. van Zalinge, R. S. J. Sparks, F. J. Cooper, D. J. Condon, Early Miocene large-volume ignimbrites of the Oxaya Formation, Central Andes. *Journal of the Geological Society* **173**, 716–733 (2016).

20. C. Wilson, Ignimbrite morphology and the effects of erosion: a New Zealand case study. *Bull Volcanol* **53**, 635–644 (1991).

21. A. BOND, R. S. J. SPARKS, The Minoan eruption of Santorini, Greece. *Journal of the Geological Society* **132**, 1–16 (1976).

22. V. V. Ponomareva, P. R. Kyle, I. V. Melekestsev, P. G. Rinkleff, O. V. Dirksen, L. D. Sulerzhitsky, N. E. Zaretskaia, R. Rourke, The 7600 (14C) year BP Kurile Lake caldera-forming eruption, Kamchatka, Russia: stratigraphy and field relationships. *Journal of Volcanology and Geothermal Research* **136**, 199–222 (2004).

23. S. YOKOYAMA, Mode of movement and emplacement of the Ito pyroclastic flow flom Aira caldera, Japan. *Tokyo Kyoiku Daigaku Science Report Sec.* **12**, 17–62 (1974).

24. D. T. Aldiss, S. A. Ghazali, The regional geology and evolution of the Toba volcano-tectonic depression, Indonesia. *Journal of the Geological Society* **141**, 487–500 (1984).

25. G. Carrasco-Núñez, M. J. Branney, Progressive assembly of a massive layer of ignimbrite with a normal-to-reverse compositional zoning: the Zaragoza ignimbrite of central Mexico. *Bull Volcanol* **68**, 3–20 (2005).

26. C. J. N. Wilson, W. Hildreth, The Bishop Tuff: New Insights from Eruptive Stratigraphy. *The Journal of Geology* **105**, 407–440 (1997).

27. M. A. Lanphere, D. E. Champion, R. L. Christiansen, G. A. Izett, J. D. Obradovich, Revised ages for tuffs of the Yellowstone Plateau volcanic field: Assignment of the Huckleberry Ridge Tuff to a new geomagnetic polarity event. *GSA Bulletin* **114**, 559–568 (2002).

28. R. A. F. Cas, H. M. N. Wright, C. B. Folkes, C. Lesti, M. Porreca, G. Giordano, J. G. Viramonte, The flow dynamics of an extremely large volume pyroclastic flow, the 2.08-Ma Cerro Galán Ignimbrite, NW Argentina, and comparison with other flow types. *Bull Volcanol* **73**, 1583–1609 (2011).

29. T. E. Jordan, B. L. Isacks, R. W. Allmendinger, J. A. Brewer, V. A. Ramos, C. J. Ando, Andean tectonics related to geometry of subducted Nazca plate. *GSA Bulletin* **94**, 341–361 (1983).

30. G. Wörner, K. Hammerschmidt, F. Henjes-Kunst, J. Lezaun, H. Wilke, Geochronology (40Ar/39Ar, K-Ar and He-exposure ages) of Cenozoic magmatic rocks from Northern Chile (18-22°S): implications for magmatism and tectonic evolution of the central Andes. *Revista geológica de Chile* **27**, 205–240 (2000).

31. M. E. van Zalinge, D. F. Mark, R. S. J. Sparks, M. M. Tremblay, C. B. Keller, F. J. Cooper, A. Rust, Timescales for pluton growth, magma-chamber formation and super-eruptions. *Nature* **608**, 87–92 (2022).

32. K. X. Whipple, G. E. Tucker, Dynamics of the stream-power river incision model: Implications for height limits of mountain ranges, landscape response timescales, and research needs. *Journal of Geophysical Research-Solid Earth* **104**, 17661–17674 (1999).

33. A. D. Howard, G. Kerby, Channel changes in badlands. *Geological Society of America Bulletin* **94**, 739–752 (1983).

34. J. Flint, Stream gradient as a function of order, magnitude, and discharge. *Water Resources Research* **10**, 969–973 (1974).

35. J. T. Hack, "Studies of longitudinal stream profiles in Virginia and Maryland" (United State Department of the Interior, 1957).

36. M. E. MORISAWA, Quantitative Geomorphology of Some Watersheds in the Appalachian Plateau. *GSA Bulletin* **73**, 1025–1046 (1962).

37. Solutions of the stream power equation and application to the evolution of river longitudinal profiles - Royden - 2013 - Journal of Geophysical Research: Earth Surface - Wiley Online Library. https://agupubs.onlinelibrary.wiley.com/doi/full/10.1002/jgrf.20031.

38. O. Korup, A. L. Densmore, F. Schlunegger, The role of landslides in mountain range evolution. *Geomorphology* **120**, 77–90 (2010).

39. K. X. Whipple, Bedrock rivers and the geomorphology of active orogens. *Annual Review of Earth and Planetary Sciences* **32**, 151–185 (2004).

40. J. D. Stock, D. R. Montgomery, Geologic constraints on bedrock river incision using the stream power law. *Journal of Geophysical Research: Solid Earth (1978–2012)* **104**, 4983–4993 (1999).

41. K. X. Whipple, N. P. Snyder, K. Dollenmayer, Rates and processes of bedrock incision by the Upper Ukak River since the 1912 Novarupta ash flow in the Valley of Ten Thousand Smokes, Alaska. *Geology* **28**, 835–838 (2000).

42. P. van der Beek, P. Bishop, Cenozoic river profile development in the Upper Lachlan catchment (SE Australia) as a test of quantitative fluvial incision models. *Journal of Geophysical Research: Solid Earth* **108**, JB002125 (2003).

43. B. Campforts, V. Vanacker, F. Herman, M. Vanmaercke, W. Schwanghart, G. E. Tenorio, P. Willems, G. Govers, Parameterization of river incision models requires accounting for environmental heterogeneity: insights from the tropical Andes. *Earth Surface Dynamics* **8**, 447–470 (2020).

44. J. R. Zondervan, A. C. Whittaker, R. E. Bell, S. E. Watkins, S. A. S. Brooke, M. G. Hann, New constraints on bedrock erodibility and landscape response times upstream of an active fault. *Geomorphology* **351**, 106937 (2020).

45. B. A. Adams, K. X. Whipple, A. M. Forte, A. M. Heimsath, K. V. Hodges, Climate controls on erosion in tectonically active landscapes. *Science Advances* **6**, eaaz3166 (2020).

46. K. L. Ferrier, K. L. Huppert, J. T. Perron, Climatic control of bedrock river incision. *Nature* **496**, 206–209 (2013).

47. C. Wobus, K. X. Whipple, E. Kirby, N. Snyder, J. Johnson, K. Spyropolou, B. Crosby, D. Sheehan, Tectonics from topography: Procedures, promise, and pitfalls. *Geological Society of America Special Papers* **398**, 55–74 (2006).

48. G. A. Ruetenik, J. D. Jansen, P. Val, L. Ylä-Mella, Optimising global landscape evolution models with ^{10}Be. *Earth Surface Dynamics* **11**, 865–880 (2023).

49. W. B. Ouimet, K. X. Whipple, D. E. Granger, Beyond threshold hillslopes: Channel adjustment to base-level fall in tectonically active mountain ranges. *Geology* **37**, 579–582 (2009).

50. R. A. DiBiase, K. X. Whipple, A. M. Heimsath, W. B. Ouimet, Landscape form and millennial erosion rates in the San Gabriel Mountains, CA. *Earth and Planetary Science Letters* **289**, 134–144 (2010).

51. M.-A. Harel, S. M. Mudd, M. Attal, Global analysis of the stream power law parameters based on worldwide 10 Be denudation rates. *Geomorphology* **268**, 184–196 (2016).

52. D. Lague, The stream power river incision model: evidence, theory and beyond. *Earth Surface Processes and Landforms* **39**, 38–61 (2014).

53. E. Marder, S. F. Gallen, Climate control on the relationship between erosion rate and fluvial topography. *Geology* **51**, 424–427 (2023).

54. D. E. J. Hobley, J. M. Adams, S. S. Nudurupati, E. W. H. Hutton, N. M. Gasparini, E. Istanbulluoglu, G. E. Tucker, Creative computing with Landlab: an open-source toolkit for building, coupling, and exploring two-dimensional numerical models of Earth-surface dynamics. *Earth Surf. Dynam.* **5**, 21–46 (2017).

55. J. S. Leonard, K. X. Whipple, Influence of Spatial Rainfall Gradients on River Longitudinal Profiles and the Topographic Expression of Spatially and Temporally Variable Climates in Mountain Landscapes. *Journal of Geophysical Research: Earth Surface* **126**, e2021JF006183 (2021).

56. K. R. Barnhart, G. E. Tucker, S. G. Doty, C. M. Shobe, R. C. Glade, M. W. Rossi, M. C. Hill, J. Geophys. Res. Earth Surf. doi: 10.1029/2019JF005287.

57. T. E. Jordan, N. E. Kirk-Lawlor, N. P. Blanco, J. A. Rech, N. J. Cosentino, Landscape modification in response to repeated onset of hyperarid paleoclimate states since 14 Ma, Atacama Desert, Chile. *GSA Bulletin* **126**, 1016–1046 (2014).

58. J. M. Shaw, L. Evenstar, F. J. Cooper, B. A. Adams, A. J. Boyce, F. Hofmann, K. A. Farley, A Rusty Record of Weathering and Groundwater Movement in the Hyperarid Central Andes. *Geochemistry, Geophysics, Geosystems* **22**, e2021GC009759 (2021).

59. F. Cooper, B. Adams, J. Blundy, K. Farley, R. McKeon, A. Ruggiero, Aridity-induced Miocene canyon incision in the Central Andes. *Geology* **44**, 675–678 (2016).

60. M. Fox, T. Bodin, D. L. Shuster, Abrupt changes in the rate of Andean Plateau uplift from reversible jump Markov Chain Monte Carlo inversion of river profiles. *Geomorphology* **238**, 1–14 (2015).

61. K. X. Whipple, B. J. Meade, Orogen response to changes in climatic and tectonic forcing. *Earth and Planetary Science Letters* **243**, 218–228 (2006).

62. T. H. Druitt, C. R. Bacon, Lithic breccia and ignimbrite erupted during the collapse of Crater Lake Caldera, Oregon. *Journal of Volcanology and Geothermal Research* **29**, 1–32 (1986).

63. H. W. Beeson, S. W. McCoy, Geomorphic signatures of the transient fluvial response to tilting. *Earth Surface Dynamics* **8**, 123–159 (2020).

64. S. Bonnet, A. Crave, Landscape response to climate change: Insights from experimental modeling and implications for tectonic versus climatic uplift of topography. *Geology* **31**, 123–126 (2003).

65. B. A. Adams, K. V. Hodges, K. X. Whipple, T. A. Ehlers, M. C. van Soest, J.-A. Wartho, Constraints on the tectonic and landscape evolution of the Bhutan Himalaya from thermochronometry. *Tectonics* **34**, 1329–1347 (2015).

66. A. Madella, R. Delunel, N. Akçar, F. Schlunegger, M. Christl, 10Be-inferred paleo-denudation rates imply that the mid-Miocene western central Andes eroded as slowly as today. *Sci Rep* **8**, 2299 (2018).

67. J. Starke, T. A. Ehlers, M. Schaller, Latitudinal effect of vegetation on erosion rates identified along western South America. *Science* **367**, 1358–1361 (2020).

68. N. M. Gasparini, K. X. Whipple, Diagnosing climatic and tectonic controls on topography: Eastern flank of the northern Bolivian Andes. *Lithosphere* **6**, 230–250 (2014).

69. C. Wobus, A. Heimsath, K. Whipple, K. Hodges, Active out-of-sequence thrust faulting in the central Nepalese Himalaya. *Nature* **434**, 1008–1011 (2005).

70. M. G. Fellin, C.-Y. Chen, S. D. Willett, M. Christl, Y.-G. Chen, Erosion rates across space and timescales from a multi-proxy study of rivers of eastern Taiwan. *Global and Planetary Change* **157**, 174–193 (2017).

71. W.-H. Hsu, T. B. Byrne, W. Ouimet, Y.-H. Lee, Y.-G. Chen, M. van Soest, K. Hodges, Pleistocene onset of rapid, punctuated exhumation in the eastern Central Range of the Taiwan orogenic belt. *Geology* **44**, 719–722 (2016).

72. N. N. Avdievitch, T. A. Ehlers, C. Glotzbach, Slow Long-Term Exhumation of the West Central Andean Plate Boundary, Chile. *Tectonics* **37**, 2243–2267 (2018).

73. M. Sdrolias, R. D. Müller, Controls on back-arc basin formation. *Geochemistry, Geophysics, Geosystems* **7**, GC001090 (2006).

74. F. Pardo-Casas, P. Molnar, Relative motion of the Nazca (Farallon) and South American Plates since Late Cretaceous time. *Tectonics* **6**, 233–248 (1987).

Acknowledgments

Funding:

AXA Research Fellowship 2017-AXA-PDOC2-036 (BAA)
Royal Society Dorothy Hodgkin Fellowship DHF\R1\180068 (BAA)
Royal Society Fellows Enhancement Award RGF\EA\181086 (BAA)
BHP Research Grant (FJC)

Author contributions:

Conceptualization: BAA, FJC, KVC
Methodology: BAA, CW
Investigation: BAA, CW
Visualization: BAA, FJC
Writing—original draft: BAA, FJC, CW, KVC
Writing—review & editing: BAA, FJC, CW, KVC

Competing interests:

Authors declare that they have no competing interests.

Data and materials availability: Codes used to produce the landscape evolution models and analyze model output, as well as the summarized data used to make all figures are available on BAA's GitHub page https://github.com/baadams/ignimbrites.

Supplementary Materials

Figs. S1 and S2 and S3
Table S1